

ANALYSIS OF THE TRANSVERSE SHIELDING PROBLEM AT PROTON ACCELERATORS USING A HADRONIC CASCADE CODE WITH LOW ENERGY PARTICLE MODULES

J.M. ZAZULA * and K. TESCH

Deutsches Elektronen-Synchrotron DESY, Notkestrasse 85, D-2000 Hamburg 52, FRG

Received 20 July 1989

Radiation protection quantities of interest (dose equivalent and absorbed dose in tissue, particle currents emerging from a shield, mean quality factors) have been obtained behind ordinary and heavy concrete of various thicknesses, at transverse directions relative to a high energy (25–800 GeV) proton beam hitting a thick iron target. The calculations were performed by using the FLUNEV program, linking the Monte Carlo hadronic cascade code FLUKA87, the EVAP-5/HETC-KFA module describing nuclear evaporation, and a low energy neutron transport module based on the MORSE code and the HILO multigroup cross section library (from 50 MeV down to thermal neutron energy). The total dose equivalents estimated by using two nearly independent methods (by multiplication of particle currents entering the tissue boundary by fluence-to-dose conversion factors, and by multiplication of absorbed doses in the tissue volume by quality factors) are in a good agreement. The neutron current and dose spectra are presented, indicating the dominance of neutrons in the 0.5–20 MeV energy range due to the evaporation process; the contributions from neutrons above 20 MeV for ordinary concrete and from neutrons below 0.5 MeV for heavy concrete are also remarkable. The dose equivalents are fitted to the simple attenuation formula suggested previously. The dose attenuation lengths are 107 g cm^{-2} for ordinary concrete and 116 g cm^{-2} for heavy concrete.

1. Introduction

For shielding calculations the actual shielding arrangement is usually simplified and reduced to typical shielding geometries. The most important case of them is the lateral shielding, a cylindrical shield parallel to and infinitely long in the direction of the primary particle beam. Other typical situations are the shielding of a target at small angles to the beam, the backstop geometry, or labyrinths and ducts. The shielding material most commonly used is concrete, sometimes iron-loaded concrete, or even pure iron is chosen. The magnitude of main interest is the total dose equivalent, it determines the thickness of the shielding wall. Other important quantities are the dose equivalents of the different radiation components, absorbed doses, particle spectra, mean quality factors and detector responses. They determine the type of health physics instruments to be used for surveying the area and for measuring personal doses. Usually the designer is concerned about the maximum of these quantities, therefore he assumes the absorption of the primary proton beam by a target thick enough to allow the complete development of the hadronic cascade but with virtually no shielding effect (the optimum target). Another assumption is a succes-

sion of thin targets producing a line source. In the present work we confine ourselves to the most important lateral concrete shielding and a thick iron absorber as an optimum target for the primary proton beam. The concrete is backed by a layer of tissue-equivalent material acting as a phantom for which we calculated the quantities of radiological interest and especially their maxima along the shielding block. The results should be valid in the beam energy range 1 GeV–1 TeV.

Clearly the most important quantity for our configuration is the total dose equivalent. Many experimental and theoretical works contribute to its determination. The most important sources of information up to beginning of 1986 are collected in refs. [1,2]. It was shown in ref. [1] that the data from:

- 1) experimental results for primary proton energies up to 24 GeV reviewed by Stevenson et al.;
- 2) measurements at energies between 200 and 800 GeV performed at the Fermi National Laboratory;
- 3) analytical calculations by O'Brien;
- 4) calculations of absorbed doses by the MC program FLUKA82 *;
- 5) the $E_p^{0.8}$ dependence of the dose equivalent derived by R.H. Thomas and S.V. Thomas can be sum-

* On leave of absence from the Institute of Nuclear Physics, Krakow, Poland.

* The last two digits enumerate succeeding versions of the Monte Carlo (MC) code FLUKA [15].

marized by the simple formula

$$H = H_0 E_p^{0.8} \frac{e^{-d/\lambda}}{r^2} \quad (1)$$

where H is the maximum value of the dose equivalent along the wall, per primary proton of energy E_p ; d is the shield thickness, and r is the transverse distance to the beam. The parameters found for ordinary concrete are: $H_0 = 1.5 \times 10^{-14}$ Sv m² and $\lambda = 107$ g cm⁻², with E_p in GeV.

Though such an agreement is satisfying eq. (1) is not the final solution of the transverse shielding problem. The works mentioned above suffer from several deficiencies: e.g., the dose equivalent could not be determined in the best possible way in every experiment; none of them report genuine shielding experiments in which different shielding thicknesses can be studied; a rather simple model of star production was the input for the analytical calculations; for the MC calculations a mean quality factor was simply assumed. In addition, eq. (1) or similar published formulas of this type (see ref. [2], chap. 4A) do not allow a simple physical interpretation, cf. ref. [3]. What we really need are better and detailed experiments at high energies. Unfortunately, the chances of such an experiment are rapidly decreasing at the existing accelerators and storage rings. An improvement of analytical methods in shielding calculations is not in sight. Therefore MC calculations are at present the only and extensively exploited tool to obtain a better insight into the physics of shielding at high energies.

The two most important analog MC programs useful for studying shielding problems at high energies are the FLUKA code developed at CERN [15] and the HETC code developed at ORNL [14]. The advantages and disadvantages of these programs are somewhat complementary. The FLUKA code has the most advanced high-energy event generator which can be used up to the TeV energy range, HETC in its hitherto released version is restricted to energies of about 3 GeV (a search for new generators is in progress [6]). In FLUKA the intranuclear cascade particles and the residual excitation energy are sampled from the semi-empirical formulas supplied with the code, whereas HETC involves a unique model for detailed MC simulation of the intranuclear cascade and evaporation processes (it is, however, considerably slower than FLUKA).

The common drawback of the hadronic cascade simulation codes is the use of a cutoff energy between 20 and 50 MeV. The main reason for this procedure is that low energy nuclear reactions are too different from those at high energies and the complicated structure of their cross sections does not allow simple model parametrizations (instead, cross sections required by neutron transport codes are retrieved from nuclear data bases).

Moreover, incorporation of these slow particles is considered to lead to prohibitively long calculation times.

The significance of the slow secondary particles for the energy deposition of hadronic cascades is commonly understood at present. Particularly in our problem and in spite of the high primary energies, all the radiological quantities of interest are supposed to be mainly due to radiation components below the usual threshold of the codes mentioned above. A simple way to deal with this problem is to use a roughly established ratio of the dose equivalent to star density or a ratio of the total neutron fluence to the high energy neutron fluence [1,2,5]. Another approach [3] is the use of a mean quality factor for the calculated absorbed dose. The HETC users (e.g. refs. [7,10]) included the low energy neutron spectra by coupling the threshold (20 MeV) neutron energy source from HETC history tapes to neutron transport codes like MORSE [16], ANISN [22] or DOT [23]. Following this approach, sophisticated code systems (e.g. CALOR [19] or HERMES [20]) have been developed by groups performing hadronic calorimeter studies. Pure neutronic codes (Monte Carlo or discrete ordinates) with a cross section data library [25] extended to a few hundred MeV have also occasionally been used for accelerator shielding calculations [11,9]. An extension of the FLUKA code to low energy neutrons, called NEUKA [21], has recently been reported, but its possible application is restricted to a uranium calorimeter design. Given current scientific collaboration, the exchange of computer codes and data between the centers and, moreover, exchange of modules between different codes becomes a quite useful practice, e.g., the high energy particle production model EVENTQ has been adopted from FLUKA, revised and incorporated into the HETC code to improve its performance at higher energies [6].

For our analysis, we have developed and tested a new version of the FLUKA code, called FLUNEV. It combines the original FLUKA87 with the evaporation module EVAP-5 taken from HETC (the KFA Jülich version [13]) and the low energy neutron cross section package MORSEC taken from the MORSE [16] MC neutron transport code. In this way it is possible to follow and score the neutrons produced in the cascade and in the nuclear deexcitation steps down to thermal energies (ten orders of magnitude in the energy scale). In contrast to the transfer of large data files between different codes in the sophisticated code systems, this linking of the modules into one program (now possible on advanced large-memory machines) enables the computer unit to transfer event data by the central core thus accelerating the jobs and making them easier to run by reducing user operations. A simplified flow diagram of the neutronic part of FLUNEV code is shown in fig. 1.

Our extensions to FLUKA87 to include the production and slowing down of neutrons below 50 MeV are described in sections 2.1 and 2.2. The FLUNEV options

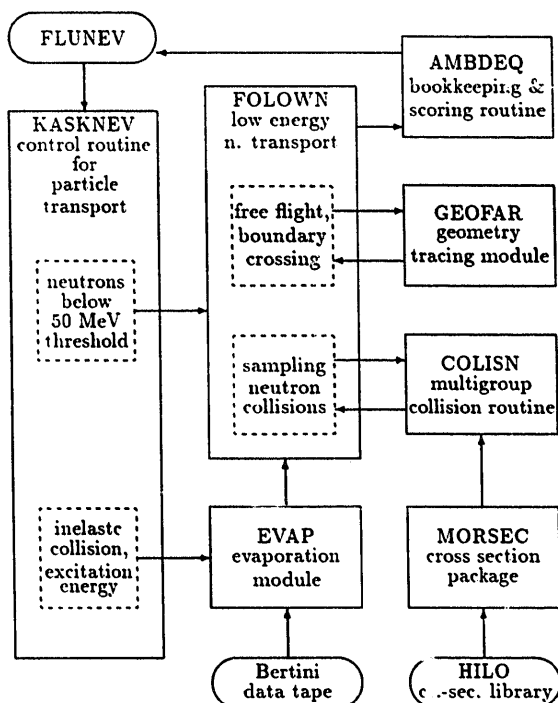


Fig. 1. Simplified flow diagram for sampling of the low energy neutrons in FLUNEV.

for scoring the dose equivalent and absorbed dose in tissue material are described in section 2.3. In sections 3.1 and 3.2 we comment on the low energy neutron cross sections used, kerma factors, fluence-to-dose conversion factors and quality factors. The next section provides the description of the geometry model, the preliminary tests and other details of the MC calculations. The results for the neutron spectra and doses behind the ordinary concrete and heavy concrete shields of different thicknesses and for different beam energies, comparison with other dose estimations and determination of relations between different quantities describing the radiation field of a hadronic cascade are discussed in section 5.

2. Extensions to the original FLUKA code

2.1. Nuclear deexcitation after inelastic interactions

For the inelastic hadron-nucleus collisions in FLUKA the energy carried off by the intranuclear cascade particles and the residual energy E_{ex} (TV in the original code and related documentation) left in a nucleus after the hadron-hadron interactions and intranuclear cascade are sampled from semi-empirical formulas. The low energy particle emission events from deexcitation of the residual nucleus are not generated by the original FLUKA model. Instead, the excitation energy is roughly divided into two parts of $\frac{1}{3}E_{\text{ex}}$ as-

sumed to be deposited in place of interaction and of $\frac{2}{3}E_{\text{ex}}$ assumed to be deposited isotropically within one inelastic interaction length of the threshold energy neutrons. The energy of particles falling down below the 50 MeV limit is deposited in the same manner. Here we should note that some other fraction should be separated which is not deposited and not taken by neutrons, but which is lost for the nuclear binding energy and excess mass effects.

Incorporation of the evaporation model provides the randomly selected yields, energies and directions of the produced neutrons, protons, and heavy fragments (α , d , t , etc.). The EVAP module is called (see fig. 1) after the inelastic interaction has taken place (except with hydrogen). The evaporation code is based on the Weisskopf theory extended by many others, finally by the KFA Jülich group [13] as a part of their HETC version, from where it was adopted by us. The updated data on nuclear masses, radii, shell and pairing energies, inverse cross sections and pre-computed functions is read from a special data set (called Bertini tape).

An excitation energy has to be provided to the EVAP module together with the mass number A and atomic number Z of a pre-evaporation nucleus. The E_{ex} value, as it is sampled by original FLUKA, has been assumed by us, until the better intranuclear cascade model is implemented in FLUKA and tested. The most difficult problem was that the mass of the excited nucleus is not defined in original FLUKA. We have recalculated it after each inelastic event using the relativistic kinematics, *postulating* the four-momentum conservation, although it has been pointed out [6] that for the FLUKA sampling model it is fulfilled only on the average (our evaporation model is clearly more exact than its input values). The total energy E_{R} (GeV) and momentum P_{R} (GeV/c) of the residual nucleus are given by:

$$E_{\text{R}} = E_1 + M_{\text{T}} - \sum_{i=1}^N E_i, \quad (2)$$

$$P_{\text{R}} = P_1 - \sum_{i=1}^N P_i, \quad (3)$$

where E_1 , P_1 is the total energy and momentum of the incident particle, E_i , P_i are the energies and momenta of the N secondaries produced in hadronic interactions and in the intranuclear cascade, and M_{T} is the target mass in GeV. The total mass of the excited nucleus is determined from:

$$M_{\text{R}}^* = \sqrt{E_{\text{R}}^2 - P_{\text{R}}^2} \quad (4)$$

and, finally, its rest mass M_{R} (GeV) and kinetic energy E_{rec} (also used as an input to EVAP, to account for anisotropic emission of evaporation products) are

Table 1
Results for particle production from the evaporation module, per inelastic interaction, averaged over the system of a 800 GeV p beam on an iron target and 100 cm concrete shield

	Initial excitation energy	Residual excitation energy	Residual recoil energy	Evaporated neutrons	Evaporated protons	Evaporated heavies
Energy ^{a)} (MeV)	136	5.3	1.6	6.5	9.0	12.2
Yield ^{b)}				4.8	0.9	1.7

^{a)} Per emitted particle.

^{b)} Per inelastic interaction.

calculated from:

$$M_R = M_R^* - E_{ex}, \quad (5)$$

$$E_{rec} = E_R - M_R^*, \quad (6)$$

where as the E_{ex} value we assume the excitation energy just sampled in FLUKA. As a test of energy and momentum balance, we additionally check (compare eqs. (4) and (5)) the following conditions:

$$E_R^2 \geq P_R^2, \quad (7)$$

$$M_R^* \geq E_{ex}, \quad (8)$$

to eliminate the rare cases in which the residual nucleus mass could not be determined at all. Fortunately, we found empirically that for the materials and energies considered (see section 4) these strange cases do not occur with a frequency higher than one per 1000 beam particles (i.e. 10^6 stars) and thus they can be neglected. For all other cases we assume that even if the A number distribution of residual nuclei obtained in such a manner (see fig. 3) is not the correct one, this uncertainty has no significant influence on the yields and energies of the

secondary particles produced. The Z number of the excited nucleus is obtained from charge conservation. The recoil energy and the residual excitation energy of the post-evaporation nucleus are also determined by EVAP.

The mean yields and energies of the particles produced in evaporation process, per inelastic high energy collision, are given in table 1. The typical evaporated neutron spectrum obtained in FLUNEV is shown in fig. 2, and the atomic mass distribution of the residual nuclei is given in fig. 3. Both the figures look reasonable and give confidence in the computational method. Table 2 presents an example of the comparison of total energy balance in the system of interest (see section 4) as calculated by the original FLUKA and by the extended version. The partition of excitation energy into different processes, when applying the EVAP module, looks different from that of the original FLUKA. Half of the initial excitation energy is spent for the nuclear binding energy, about 30% for evaporated charged particles, recoil and residual excitation, and only about 20% is taken away by about 5 evaporated neutrons.

Table 2
Distribution of initial beam energy to different processes and particles in the original FLUKA and FLUNEV, for the system containing an iron target and a 100 cm lateral concrete shield

	$E_p = 3 \text{ GeV}$		$E_p = 800 \text{ GeV}$	
	FLUKA86	FLUNEV	FLUKA86	FLUNEV
Ionization losses	27.7%	28.2%	10.2%	9.7%
El.-magn. cascade	18.6%	17.9%	57.9%	52.2%
$E < 50 \text{ MeV}$ particles	7.9%	8.2%	3.0%	2.9%
Escaping particles	13.7%	11.0%	16.7%	23.7%
Excitation ^{a)}	32.2%	–	9.6%	–
Evaporated n	–	6.9%	–	1.8%
Evaporated p	–	2.4%	–	1.0%
Evap. heavies	–	5.7%	–	1.5%
Residual recoil	–	0.4%	–	0.1%
Res. excitation	–	1.1%	–	0.4%
Binding en. losses	–	18.1%	–	4.8%
Sum ^{b)}	100.1%	99.9%	97.4%	98.1%

^{a)} Original FLUKA model of energy deposition.

^{b)} Some small fraction is usually missed in FLUKA.

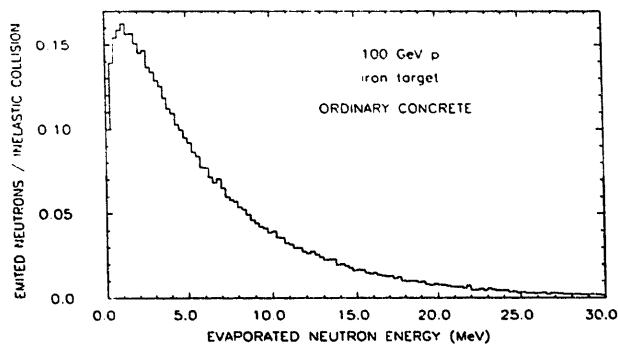


Fig. 2. Averaged spectrum of evaporated neutrons, per inelastic interaction, for 100 GeV p on an iron target and 100 cm concrete shield.

Nearly the same amount of the excitation energy is deposited locally by FLUKA and FLUNEV. However, the total energy of evaporated neutrons is considerably smaller (a factor of 3) in the latter. The resulting effect is partially compensated by the additionally calculated transport of these particles, since the emitted neutrons penetrate distances much larger than one neutron inelastic interaction length (as assumed in FLUKA).

2.2. Low energy neutron transport module

The special subroutine FOLOWN has been written by us to follow low energy neutrons within the FLUNEV code. It is called (see fig. 1) from the particle transport controlling subroutine KASKNEV (corresponding to the original KASKAD) each time the neutron falls below the 50 MeV energy limit, or when it is produced by an evaporation process. $\frac{2}{3}$ of the energy of other stable particles falling below the threshold is also converted to one neutron in a direction sampled from an isotropic distribution (as in original KASKAD).

Neutrons are tracked in FOLOWN between the collisions and region boundaries using the original FLUKA geometry package (GEOFAR and related routines). Their energy range from 50 MeV to 0.4 eV (assumed for

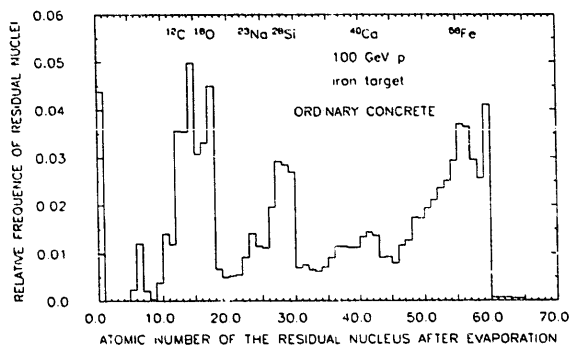


Fig. 3. Atomic mass distribution of residual nuclei after evaporation, for 100 GeV p on an iron target and 100 cm concrete shield.

thermal neutrons) is divided into intervals (the energy groups). Changes of the energies and directions in subsequent collisions are controlled in FOLOWN by calling the COLISN subroutine, adapted from the MORSE multigroup code. The special external data set called the multigroup library is retrieved by the XSECFL subroutine adapted from the MORSEC package, processing the data for the core arrays suitable for the MC game. The library tape contains the cross sections and energy transfer probabilities averaged over the energy groups and for most of the neutron-induced nuclear reactions for a given isotope. The energy deposited by the charged particles released in these reactions is described by multigroup k_{eff} factors (see the next section).

Sampling low energy neutron collisions in large systems is a very time consuming process. In the case of our transverse shielding geometry it is fortunately not necessary to do this in the whole system when calculating doses outside a shield. The spectra of neutrons are of interest only in the outermost shielding layer, when they emerge through the concrete boundary, and eventually in the exposed phantom. Therefore an effective FLUNEV option which saves computer time, is to specify the particular user-defined geometry regions in which neutrons are transported down to thermal energy. Neutrons in the thermal group are assumed to be absorbed within one diffusion length from the position where they have been slowed down (if they do not escape by chance). For the regions other than those defined by a user neutrons are tracked only above a particular energy limit E' that is also optionally defined, and they are assumed to be absorbed within the next interaction length (corresponding to E') when falling below it (if they do not escape or reach the region of interest by chance). Using this option only the most penetrating component is propagated through a bulk shield, and the component which is likely to be absorbed before contributing to the dose is neglected.

Both these new FLUNEV options define the problem-dependent cutoffs for the neutron histories, other user-input parameters are not required when compared with FLUKA. Note that the parameters of these options are problem-dependent. The pre-specified regions should have large enough dimensions (at least comparable with the slowing down length of the fast neutron component) to assure the equilibrium character of the relevant neutron spectra. The E' energy limit should be set up below the energy range for which the neutron attenuation lengths are substantially longer than for lower energies, thus it also depends on the material. Except of the nonanalog absorption (i.e. multiplication of a particle weight by the nonabsorption probability at subsequent collisions instead of killing it randomly), all the advanced biasing techniques available in the MORSE code (the Russian roulette, splitting, path length stretching and importance sampling) have tem-

porarily been abandoned in FLUNEV, since some preliminary trials showed that they did not provide apparent benefits for statistical errors and computing times. Their physical and statistical background require further investigations.

2.3. Scoring of the dose equivalent and absorbed dose in tissue

Scoring of the dose contributions from different radiation components in a tissue-equivalent material is the essential task performed by the FLUNEV program, when applied to the radiation protection area. The new subroutine AMBDEQ was written to extend the original FLUKA options by calculating the absorbed doses and dose equivalents from different radiation components for user-specified regions, and by bookkeeping the fluence spectra and the dose spectra of neutrons and other particles. In general, the methods of estimation depend on the quantity of interest, on the physical processes, on the type of particles and on the energy range, as is described below.

2.3.1. Absorbed dose

The scoring of the absorbed dose directly from particles above 50 MeV has not been changed with regard to the FLUKA defaults. Their deposited energy consists of two components:

- 1) Ionization energy losses of charged particles: the distance between subsequent collisions is divided into steps, and at each step the energy of particle is reduced according to the stopping power formula; the energy lost is deposited in the midpoint of the step.
- 2) The energy deposited from the electromagnetic cascade is sampled from semi-empirical formulas describing the radial and longitudinal distributions (or the EGS system [18] is called).

One part of the absorbed dose from high energy neutrons is included in the first component as the energy of their charged secondaries, another part is due to the deexcitation of the residual nuclei after the neutron inelastic interactions. The excitation energy together with the energy of particles falling below the threshold is the third component of the absorbed dose calculated by the original FLUKA.

In the FLUNEV version of FLUKA, an inelastic collision is followed by the evaporation process and the energy of evaporated protons, heavy fragments (α , d, t, ^3He) and the recoil energy increase the deposited energy counter at the site of an interaction. Another fraction of the energy released is taken by evaporated neutrons and further transported through the system – either escaping or becoming deposited elsewhere. The remaining part of E_{ex} is lost, either as the nuclear binding energy, or as deexcitation photons from a nucleus residual after

the evaporation, escaping from outer regions of the system and thus not counted.

The low energy component of the absorbed dose calculated by FLUNEV is due to neutron reactions (elastic and inelastic scattering, (n, γ) and $(n, \text{charged})$ capture, $(n, 2n)$, fission etc.), contributing to the dose by depositing the kinetic energy of secondary charged particles and the recoil energy of a residual nucleus or fragments in place of a reaction. The corresponding amount of energy is scored after each neutron interaction takes place, using the collision density estimate of the neutron fluence multiplied by the relevant kerma factor (see section 3.1 for the source of data), averaged over the neutron energy group and over most of the nuclear reactions occurring with a given element. The thermal neutron energy is totally absorbed within one diffusion length calculated for that medium. Note that the γ -ray energy from inelastic neutron scattering and radiative capture has not been included in the absorbed energy. Also the decay energy from the eventually produced radionuclides is assumed to escape the tissue regions by γ radiation.

2.3.2. Dose equivalent

An estimation of the dose equivalent can be accomplished in FLUNEV by using the following two nearly independent methods:

- (1) By multiplying the absorbed dose in the tissue-equivalent material by quality factors. Each time the energy deposited in the tissue region is incremented by one of the contributions described above, the corresponding increment in the dose equivalent is obtained by applying the quality factor according to the type and energy of the contributing particle (see next section for comments on the data).
- (2) By multiplying the particle current entering the tissue region by the relevant fluence-to-dose conversion factor (see next section for data applied). The particles contributing here are the neutrons (over the whole energy range), high energy protons and charged pions; the current of the short-range charged particles is negligible. An amount of the dose equivalent is scored each time a particle of the type indicated above crosses the tissue region boundary from outside.

The second method of calculating the dose equivalent is worth further comments. The mentioned conversion factors had been obtained for a particularly defined phantom in a particularly defined radiation field – when using the coefficients one should possibly achieve the same geometrical configuration and other conditions. In general, it is not clear if the quantity to be folded by conversion factors is the angular-integrated particle fluence Φ at the boundary.

$$\Phi(r, E) = \int_{n \cdot \Omega > 0} d\Omega \phi(r, \Omega, E), \quad (9)$$

or the angular-integrated particle current J through the boundary:

$$J(\mathbf{r}, E) = \int_{\mathbf{n} \cdot \boldsymbol{\Omega} > 0} d\boldsymbol{\Omega} (\mathbf{n} \cdot \boldsymbol{\Omega}) \phi(\mathbf{r}, \boldsymbol{\Omega}, E), \quad (10)$$

where the angular fluence ϕ is the number of particles crossing the unit area perpendicular to the particle direction vector $\boldsymbol{\Omega}$, and \mathbf{n} is the unit vector normal to the scoring surface S at \mathbf{r} and directed into the phantom. Although the fluence and current have the same unit, the inverse of an area, they have somewhat different physical meanings. The current provides a number of particles crossing the unit area of a given surface S which has a fixed orientation in space. The fluence, however, provides a number of particles crossing the unit areas related to surfaces S' at the same position, but with orientation varying to be always perpendicular to the direction of the scored particle. Thus in MC codes the sum of weights w_i of particles crossing the fixed region boundary S provides a useful estimate of the surface-averaged current through S :

$$\bar{J}_S \approx \frac{1}{MA} \sum_{i=1}^N w_i, \quad (11)$$

where M is the number of primary particles and A is the area of S . However, for estimating the fluence when crossing the same boundary, another area $A' = A \mathbf{n} \cdot \boldsymbol{\Omega}_i$ (projection of the S on the S' perpendicular to $\boldsymbol{\Omega}_i$) should be chosen for each particle direction, thus the particle weight is divided by the cosine of an angle between its actual direction and the vector normal to the boundary:

$$\bar{\Phi}_S \approx \frac{1}{MA} \sum_{i=1}^N \frac{w_i}{\mathbf{n} \cdot \boldsymbol{\Omega}_i}, \quad (12)$$

(note the singularity of this estimate for the particle direction parallel to the boundary). As a consequence, one gets the same value of both the quantities for a particle field collimated perpendicularly to the boundary, but the current is half the fluence value for an isotropic field, and zero current is obtained for a non-zero fluence, if the particles are collimated parallel to the boundary. Since particles directed parallel to the tissue boundary will not affect the dose equivalent even if they have a non-zero fluence, using the current entering the tissue region seems to be the best choice for estimating the dose equivalent:

$$D = \int dE K(E) \int_S dS J(\mathbf{r}, E), \quad (13)$$

where $K(E)$ are the conversion factors. For one case (100 GeV proton beam and 100 cm ordinary concrete shield) we performed the dose equivalent calculation using the same conversion factors and both the quantities mentioned above, either the fluence or the current.

For the high energy neutrons ($E > 50$ MeV), the component for which a higher angular anisotropy is expected, the dose equivalent estimated from the current was only 23% lower than the dose estimated from fluence (the ratio averaged over 4 tissue regions, at different angles to the primary beam) whereas for the low energy neutrons ($E < 0.5$ MeV) the mean ratio of the estimates from current and from fluence was 54% which is close to the factor 0.5 expected for an isotropic field.

3. Comments on data used

3.1. Multigroup neutron cross sections and kerma factors

Usually cross section libraries interfaced to neutron transport codes contain data only up to 20 MeV, which is the upper energy limit of the ENDF/B Evaluated Neutron Data Files [24]; there are only a few data sets extended to higher neutron energies. The most advanced is the HILO package, existing in two versions; the more recent version [26] involves some essential corrections relative to the older one [25] and includes data for more elements than are useful for radiation protection applications. However, it is distributed at present only to USA users*, and up to now we have been restricted to using the old version in our work.

HILO is the multigroup library of 66 neutron groups covering an energy range from thermal to 400 MeV, coupled with 21 γ groups from 10 keV to 15 MeV. The group structure can be found in references. For our purpose, we used only 45 neutron groups below the 50 MeV cutoff of FLUKA, and the secondary γ rays were not considered. At present data for the following 8 elements are available in FLUNEV: H, C, O, Al, Si, Fe, W and Pb. Setting up the concrete constituents (see section 4), we assumed somewhat arbitrarily that for low energy neutrons the small percentages of Na atoms are equivalent to Si, and of Ca, Mn and Mg atoms are equivalent to Al. HILO contains the coefficients for anisotropic cross sections up to P_3 order of the Legendre expansion. However, for the first calculations with the FLUNEV system presented here we decided to use only the first two (P_0 and P_1) terms, since more coefficients need much more computer time and core, and we could expect that other uncertainties in our calculations (e.g. evaporated neutron yields, treatment of threshold particles, some lacking elements, accuracy of kerma and conversion factors etc.) are larger than uncertainties due to neglecting higher order terms, especially at low en-

* Release of the HILO86 package and the new ENDF/B-VI data base is expected in 1989 (private communication from Radiation Shielding Information Center, ORNL, USA).

Table 3
Comparison of macroscopic neutron kerma factors used in the FLUNEV code and given by Caswell [12]

Element:	Neutron kerma factors (rad cm ²)						
	H	C	O	Al	Si	Fe	Tissue
<i>E</i> = 25 MeV							
FLUNEV	0.455-07 ^{a)}	0.511-08	0.406-08	0.216-08	0.265-08	0.128-08	0.838-08
Caswell	0.458-07	0.452-08	0.270-08	0.115-08	0.167-08	0.999-09	0.733-08
<i>E</i> = 0.5 MeV							
FLUNEV	0.129-07	0.151-09	0.178-09	0.332-10	0.283-10	0.735-11	0.145-08
Caswell	0.147-07	0.186-09	0.991-10	0.368-10	0.322-10	0.848-11	0.158-08
<i>E</i> = 10 eV							
FLUNEV	0.580-12	0.170-11	0.148-14	0.689-11	0.768-13	0.317-13	0.270-12
Caswell	0.128-11	0.611-14	0.278-14	0.279-14	0.267-14	0.111-13	0.145-11

^{a)} Read as 0.455×10^{-7} .

ergies. The preference of the fast particle forward directions to the shield boundary is preserved by the original transport module above 50 MeV. After retrieving the library by the XSECFL processing routine, adapted from the MORSEC package, the data arrays, used for sampling the low energy neutron track lengths and collisions, contain the following information for each neutron group: the total cross section, the non-absorption probability, and the downscatter probabilities to lower energy groups together with one mean polar angle of scattering (in laboratory system) for transfer to each lower energy group, averaged over all neutron reactions.

The multigroup kerma factors used to estimate the absorbed dose from low energy neutrons (see section 2.3) had been obtained from previous works [11,10]. There are two sources of these data. Below 20 MeV, they had been calculated from ENDF/B-IV data files using the MACK code [17] and then collapsed to the HILO group structure. Above 20 MeV, the kermas had been obtained using the intranuclear-cascade-evaporation model of HETC code for monoenergetic neutron beams on thin targets, and scoring the energy of secondary charged particles. Table 3 contains a comparison of the macroscopic kerma factors used by us with another data set published by Caswell [12], for 6 elements and for a tissue material, at 3 neutron energies. They are consistent within a factor of 2 for H, O and Fe, and they agree within the same factor for tissue. For other elements large discrepancies can be observed at the lowest energy of 10 keV (fortunately not so important for calculating the doses in our case). For possible explanations one may consider that our data have been group-averaged, at 300 K temperature, and Caswell gives point values, at 0 K. Differences between the pointwise and group data could be substantial in the case of resonances. Some other details of the treatment of the particular nuclear reactions are also different in MACK code and Caswell's method. Moreover, the energy range just above 20 MeV seems to be rather low

for the calculations with HETC models. Note also that we assumed the isotopic composition of the tissue (see table 4) to be simpler than that given in Caswell's paper.

3.2. Fluence-to-dose conversion factors and quality factors

As described in section 2.3, we used the fluence-to-dose conversion factors for one method of calculating the dose equivalent and the quality factor for the other. There are several published sets of such factors applicable for different geometries of a radiation field and a phantom, and for the most important particles. In ICRP Publication 21 [28] data are given for a plane parallel beam of particles with energies up to 3 GeV incident normally on a 30 cm thick layer of tissue-equivalent material. The more recent ICRP Publication 51 [29]

Table 4
Densities and elemental compositions of materials used in calculations

Material	Ordinary concrete	Heavy concrete	Tissue equivalent.
Density (g cm ⁻³)	2.5	3.7	1.0
H	1.0% ^{a)}	0.4%	10.1%
C	1.0%	-	12.4%
O	53.0%	34.4%	77.5%
Na ^{b)}	2.0%	-	-
Mg ^{c)}	-	1.9%	-
Al	3.0%	1.0%	-
Si	34.0%	6.8%	-
Ca ^{c)}	4.0%	4.8%	-
Mn ^{c)}	-	0.1%	-
Fe	2.0%	50.5%	-

^{a)} Per cent by weight.

^{b)} Approximated by Si for low energy neutrons.

^{c)} Approximated by Al for low energy neutrons.

Table 5

Maximum dose equivalent H outside the lateral concrete and heavy concrete shields, obtained from test calculations for various parameters E_p , d , E' and d'

Ordinary concrete				Heavy concrete			
$E_p = 800 \text{ GeV}$ $d = 100 \text{ cm}$ $d' = 20 \text{ cm}$		$E_p = 100 \text{ GeV}$ $d = 200 \text{ cm}$ $E' = 20 \text{ MeV}$		$E_p = 100 \text{ GeV}$ $d = 100 \text{ cm}$ $d' = 20 \text{ cm}$		$E_p = 100 \text{ GeV}$ $d = 100 \text{ cm}$ $E' = 10 \text{ keV}$	
$E'(\text{MeV})$	$H(\text{Sv})$	$d'(\text{cm})$	$H(\text{Sv})$	$E'(\text{MeV})$	$H(\text{Sv})$	$d'(\text{cm})$	$H(\text{Sv})$
50	4.0–14 ^{a)}	30	3.3–16	20	3.4–15	40	4.9–15
1	4.5–14	50	3.5–16	0.001	3.7–15	60	4.6–15

^{a)} Read as 4.0×10^{-14} .

gives data for a slab phantom or a 30 cm sphere (in some cases subdivided into an outer shell of 1 cm thickness and the remaining core) and for parallel or isotropic fields; the maximum energy is 100 GeV. Stevenson collected in [5] the conversion factors for neutrons, protons and charged pions up to 10 TeV; for neutrons up to 20 MeV they refer to the ambient dose equivalent – the dose equivalent in the 30 cm sphere at a depth of 1 cm in an aligned and expanded field (see ref. [30]); for higher neutron energies he gave the mean data compiled from 6 calculations using the 30 cm slab and assuming normal incidence.

It is not easy to select the data sets which are best applicable to our situation. We have the 20 cm thick cylindrical layer of a tissue-equivalent material, and the incoming radiation field is neither isotropic nor aligned. We decided to use Stevenson's conversion factors; they are in agreement (within 10%) with the data of [28] and with the deep dose equivalent index from a plane parallel field [29]; for higher neutron energies they are about 30% lower than the conversion factors of [28] and the maximum dose equivalent in the 30 cm sphere given in [29]. Moreover, by using the current instead of the fluence, we restrict the angular distributions of the radiation emerging from the shield to the component perpendicular to the tissue boundary which corresponds to the requirement of an aligned field.

The same data sets of refs. [28,29] were considered for our quality factors for neutrons, protons and pions, we simply took the mean of them. A quality factor of 20 was assumed for evaporated heavy fragments and residual recoiling nuclei. For the energy deposited by the electromagnetic cascades the quality factor is 1. We believe that the errors associated with the use of the factors described above are not larger than other systematic errors of our calculations.

4. The geometry model and further details of the calculations

Our simple model used for calculations consists of three media: the iron target, the concrete or heavy

concrete shield and the tissue layer outside the shield. The material densities and elemental compositions are listed in table 4. The cylindrical geometry model of the transverse shielding arrangement is shown in fig. 4. The target dimensions were fixed after some trial runs of the code indicating that such a length and diameter result in a maximum dose equivalent outside a 100 cm concrete shield for the highest considered beam energy of 800 GeV. The two lower energies considered were 100 GeV and 25 GeV. The shield thickness d was varied between 100 and 250 cm for concrete, and between 50 and 200 cm for heavy concrete, for each primary energy. The system is divided into four regions of 1 m length in the beam direction in order to find the maximum of the dose equivalent in the tissue layer.

As explained in section 2.2, neutrons are followed down to thermal energy only in some pre-specified regions. For our shielding problem these regions are the outermost layer of the concrete of thickness d' (see fig. 4) and the tissue layer. In the remaining part of the system neutrons are considered above a cutoff energy E' . These two parameters were varied to minimize the computer time without affecting the results. Some results of test runs with different d' and E' are given in table 5. For the iron-loaded heavy concrete the tested E' value is much lower than for the ordinary concrete since in iron the neutron attenuation lengths are known

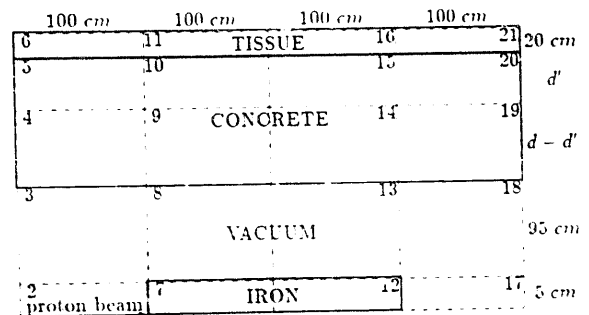


Fig. 4. Cylindrical geometry model of the shielding arrangement assumed for calculations. Solid lines are material boundaries, dashed lines are region boundaries; region numbers are indicated in top corners.

Table 6
Final run parameters for FLUNE^V Monte Carlo calculations
($E_p = 25, 100, 800$ GeV)

Ordinary concrete $E' = 20$ MeV			Heavy concrete $E' = 10$ keV		
d (cm)	d' (cm)	t (min)	d (cm)	d' (cm)	t (min)
100	30	20	50	40	20
150	40	40	100	40	40
200	50	60	150	50	60
250	60	75	200	60	75

to be large in the keV region. The final values of the two parameters are shown in table 6.

The evaporation module in FLUNE^V is called everywhere after the inelastic collisions. We observed that the excess computer time for simulation of the nuclear

deexcitation processes does not exceed 25%, compared with original FLUKA runs. For our configuration, the low energy neutron transport module additionally increased the computing times per beam particle by about 30%. The IBM-3081 machine time limits for long jobs producing the results presented in the next section are also included in table 6. The sampled primary beam particles were divided into batches, of 10 protons per each batch, in order to estimate the statistical errors from the standard deviations of the results obtained from single batches. The numerous neutrons produced by evaporation efficiently reduce the statistical errors in fluences and doses due to the low energy component, when compared to errors of quantities due to high energy particles, even at large depths. The mean time for a cascade from one beam proton depends much more on the incident energy (and thus on the total number of cascade particles produced) than on the shield thickness. Thus the total numbers of sampled

Table 7
Example results for the radiation protection magnitudes obtained from a single run of the FLUNE^V code (100 GeV p/100 cm ordinary concrete)

Region number: ^{a)}	6	11	16	21	6	11	16	21
	Particle currents entering reg. (cm ⁻²)				Absorbed dose (Gy)			
e.-m. cascade:	^{b)} -	-	-	-	2.82-17 ^{c)}	1.17-16	1.12-16	1.36-16
High en. + evap. p:	2.01-08	0.0	4.06-08	6.09-08	6.70-17	8.30-17	8.17-17	1.16-16
π^+ ($E > 50$ MeV):	0.0	2.03-08	4.06-08	6.09-08	9.71-18	7.52-18	1.22-17	5.03-17
π^- ($E > 50$ MeV):	0.0	4.06-08	2.03-08	2.03-08	1.27-18	1.75-17	1.62-17	7.14-18
Evap. $\alpha, d, t, ^3\text{H}$ + rec.:	^{d)} -	-	-	-	1.80-17	3.30-17	4.40-17	1.80-17
High en. n ($E > 50$ MeV):	1.22-06	3.71-06	4.85-06	4.89-06	^{e)} -	-	-	-
n(50 MeV > $E > 20$ MeV):	5.21-07	1.25-06	1.45-06	1.09-06	5.71-17	1.52-16	1.29-16	1.29-16
n(20 MeV > $E > 500$ keV):	1.95-06	6.26-06	8.50-06	5.54-06	9.89-17	3.79-16	3.74-16	3.28-16
n(500 keV > $E > 0.4$ eV):	2.96-06	7.66-06	1.10-05	9.13-06	5.34-17	2.65-16	3.05-16	2.17-16
thermal n ($E < 0.4$ eV):	1.50-07	2.82-07	2.28-07	2.56-07	7.15-19	3.86-18	5.75-18	3.98-18
Sum for all n:	6.79-06	1.92-05	2.60-05	2.09-05	2.10-16	8.01-16	8.14-16	6.77-16
Sum for all part.:	6.81-06	1.92-05	2.61-05	2.11-05	3.34-16	1.06-15	1.08-15	1.00-15
	Dose eqv. (Sv) est. by conv. factors				Dose eqv. (Sv) est. by qual. factors			
e.-m. cascade:	^{f)} 2.82-17	1.17-16	1.12-16	1.36-16	2.82-17	1.17-16	1.12-16	1.36-16
high en. + evap. p:	4.32-17	0.0	4.85-17	6.98-17	1.00-16	1.25-16	1.23-16	1.73-16
π^+ ($E > 50$ MeV):	0.0	2.79-17	5.78-17	8.53-17	9.80-18	1.03-17	1.27-17	6.37-17
π^- ($E > 50$ MeV):	0.0	5.55-17	2.79-17	2.70-17	2.66-18	1.51-16	1.56-16	1.43-17
evap. $\alpha, d, t, ^3\text{H}$ + rec.:	^{c)} -	-	-	-	3.61-16	6.59-16	8.80-16	3.61-16
High en. n ($E > 50$ MeV):	3.98-15	1.22-15	1.60-15	1.63-15	^{d)} -	-	-	-
n(50 MeV > $E > 20$ MeV):	2.68-16	6.52-16	7.83-16	5.58-16	3.17-16	8.45-16	7.31-16	7.15-16
n(20 MeV > $E > 500$ keV):	7.65-16	2.49-15	3.32-15	2.22-15	8.05-16	3.20-15	3.23-15	2.80-15
n(500 keV > $E > 0.4$ eV):	1.32-16	4.99-16	6.36-16	5.29-16	3.91-16	1.92-15	2.10-15	1.48-15
Thermal n ($E < 0.4$ eV):	1.56-18	2.94-18	2.37-18	2.66-18	2.00-18	1.08-17	1.61-17	1.12-17
Sum for all n:	1.57-15	4.86-15	6.35-15	4.93-15	1.52-15	5.98-15	6.08-15	5.01-15
Sum for all part.:	1.61-15	4.94-15	6.48-15	5.12-15	2.02-15	7.04-15	7.36-15	5.75-15

^{a)} See fig. 4 for region description.

^{b)} Not calculated here.

^{c)} Read as 2.82×10^{-17} .

^{d)} Not occurring here.

^{e)} Included in absorbed dose of charged secondaries.

^{f)} Included from absorbed dose.

beam protons, limited by the computing times, were different for each run.

5. Results

5.1. Basic results

The basic results from a single run of the FLUNEV code, concerning the radiation protection magnitudes, are presented in table 7 as an example. Similar data for all 24 calculated cases (4 shield thicknesses – 3 beam energies – 2 shielding materials) and other results from the runs are available on request from the authors.

The quantities of interest are the particle currents entering tissue regions, the absorbed doses and the dose equivalents estimated using either the fluence-to-dose conversion factors or the quality factors, for several radiation components, versus the geometry region, shield thickness, beam energy and shielding material. The significant components calculated are electromagnetic cascade particles, protons from high energy interactions and from evaporation, charged pions, evaporated heavy fragments and recoiling nuclei, and neutrons. For neutrons, as the most important particles at directions transverse to the beam axis, we have distinguished the following energy ranges: high energy neutrons above 50 MeV, fast neutrons between 50 MeV and 20 MeV, intermediate energy neutrons between 20 and 0.5 MeV, slow neutrons below 500 keV and a single thermal neutron group below 0.4 eV. These limits were chosen

according to the requirements of practical dosimetry: 0.5 MeV, 20 MeV and 50 MeV are the thresholds of the nuclear emulsion dosimeter, the ^{11}C method and the Bi fission counter, respectively. The results in table 7 are presented for 4 regions of the tissue layer (see fig. 4) corresponding to different angular intervals relative to the beam axis: about 120° (reg. 6), about 90° (reg. 11), about 60° (reg. 16) and about 45° (reg. 21). The maxima of the quantities along the z axis result from two competing effects, the production of secondary particles peaked in the forward direction and the increasing effective shield thickness; these maxima usually occur in reg. 16.

The particle type scored in the currents emerging from a shield are the high energy protons, charged pions and neutrons – only these particles have the abundances, lifetimes and ranges to appear at lateral directions (and the fluence-to-dose conversion factors are available only for them). The currents of protons and pions are 3 orders of magnitude lower than the neutron currents. They show up only in the regions most forward to the beam direction and outside the thinnest layers of the concrete, and only occasionally outside the heavy concrete shield. Their data in table 7 are only very approximate.

5.2. Compilation of radiological quantities

The next two tables, tables 8 and 9, provide all the main quantities of interest: neutron currents, absorbed energies and dose equivalents, estimated in reg. 16, for

Table 8

Star densities S , total particle currents J , total absorbed doses D , neutron dose equivalents H_n and total dose equivalents H_J and H_D , for tissue reg. 16, per primary p, behind ordinary concrete shields

d (cm)	S (cm^{-3})	J (cm^{-2})	D (Gy)	$H_n^{a)}$ (Sv)	$H_J^{b)}$ (Sv)	$H_D^{c)}$ (Sv)
$E_p = 25 \text{ GeV}$						
100	2.0–08 ^{d)}	9.6–06	4.5–16	2.4–15	2.5–15	3.1–15
150	4.6–09	2.3–06	8.2–17	4.9–16	5.0–16	5.8–16
200	8.3–10	5.6–07	2.0–17	1.1–16	1.1–16	1.2–16
250	2.8–10	1.1–07	3.1–18	2.0–17	2.0–17	2.4–17
$E_p = 100 \text{ GeV}$						
100	3.3–08	2.6–05	1.1–15	5.4–15	6.5–15	7.4–15
150	1.3–08	6.3–06	2.4–16	1.5–15	1.5–15	1.6–15
200	3.2–09	1.5–06	6.4–17	3.3–16	3.4–16	4.2–16
250	2.9–10	3.5–07	1.0–17	6.9–17	6.9–17	6.8–17
$E_p = 800 \text{ GeV}$						
100	2.6–07	1.4–04	6.4–15	5.5–14	3.6–14	4.4–14
150	5.1–08	3.2–05	1.4–15	7.6–15	7.7–15	9.7–15
200	1.3–08	8.2–06	2.9–16	1.8–15	1.8–15	2.4–15
250	0.0	2.2–06	6.5–17	5.2–16	5.2–16	4.9–16

^{a)} From neutrons, estimated using current and conversion factors.

^{b)} Total, estimated using current and conversion factors.

^{c)} Total, estimated using absorbed dose and quality factors.

^{d)} Read as 2.0×10^{-8} .

Table 9

Star densities S , total particle currents J , total absorbed doses D , neutron dose equivalents H_n and total dose equivalents H_J and H_D , for tissue reg. 16, per primary p, behind heavy concrete shields

d (cm)	S (cm^{-3})	J (cm^{-2})	D (Gy)	H_n ^{a)} (Sv)	H_J ^{b)} (Sv)	H_D ^{c)} (Sv)
$E_p = 25$ GeV						
50	7.5-08 ^{d)}	1.2-04	2.4-15	1.8-14	1.8-14	1.7-14
100	1.3-08	1.0-05	2.6-16	1.8-15	1.8-15	1.9-15
150	1.9-09	1.3-06	3.3-17	2.4-16	2.4-16	2.4-16
200	0.0	2.7-07	7.7-18	4.6-17	4.6-17	5.5-17
$E_p = 100$ GeV						
50	1.4-07	3.4-04	6.4-15	4.8-14	4.9-14	4.3-14
100	4.2-08	3.1-05	8.7-16	5.2-15	5.2-15	6.6-15
150	2.2-09	4.3-06	8.0-17	7.1-16	7.1-16	5.5-16
200	9.6-10	7.3-07	1.8-17	1.4-16	1.4-16	1.5-16
$E_p = 800$ GeV						
50	1.0-06	2.0-03	4.5-14	3.0-13	3.1-13	3.1-13
100	1.3-07	1.9-04	4.9-15	3.4-14	3.5-14	3.7-14
150	1.7-08	2.0-05	4.6-16	3.0-15	3.0-15	3.0-15
200	2.8-09	3.0-06	8.8-17	5.0-16	5.0-16	4.1-16

^{a)} From neutrons, estimated using current and conversion factors.

^{b)} Total, estimated using current and conversion factors.

^{c)} Total, estimated using absorbed dose and quality factors.

^{d)} Read as 7.5×10^{-8} .

the concrete and heavy concrete shields of different thicknesses and for different beam energies; the star densities in tissue have also been included for completeness. The currents and doses from other than the neutron components are below the limits of statistical accuracy (see the following tables for errors). The dose equivalents calculated by both independent methods (see section 2.3 and the discussion below) are in good agreement, within the error bounds.

The mean quality factors were obtained as the ratios of the total dose equivalents to the total absorbed doses. They do not change significantly with the region number, shield thickness, beam energy and the shielding material. The average values are: 7.3 ± 0.5 for the total neutron component and 7.2 ± 1.0 for all the considered particles.

5.3. Neutron spectra

The histograms for neutron current and corresponding neutron dose equivalent spectra are presented in figs. 5-7. The smooth curve at the upper plot of fig. 5 has been included for comparison with our spectrum (histogram) with the neutron spectrum calculated by O'Brien [31] (curve, normalized to the histogram) for aluminium with 16% water content. No essential differences of the plotted shapes can be observed when varying the shield thicknesses (fig. 5) and beam energies (fig. 6) within the ranges of our parameters, thus for a comparison of the spectra for both kinds of concrete (fig. 7) the histograms have been normalized to unity

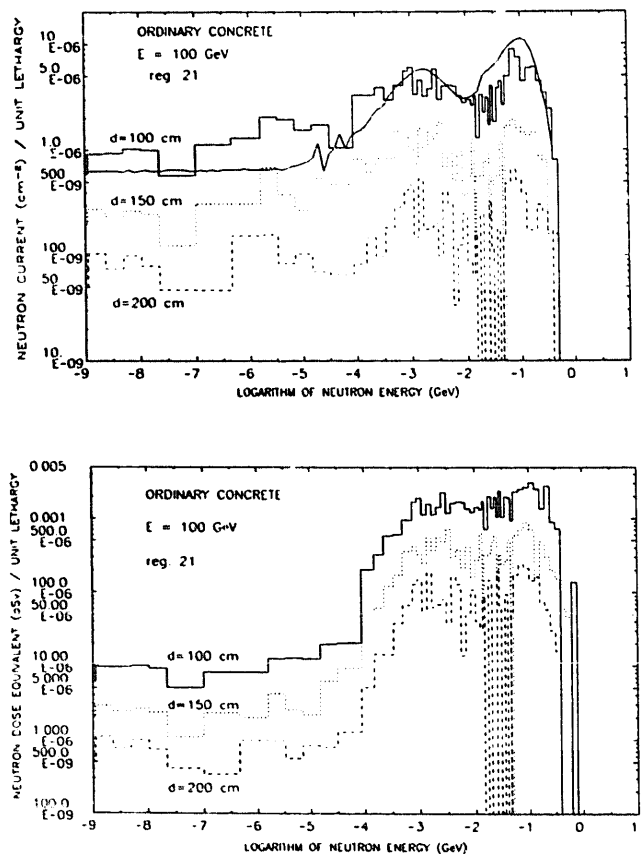


Fig. 5. Comparison of neutron current spectra and neutron dose spectra, normalized per primary proton, for 3 different thicknesses of the shield. The smooth curve added to the upper histogram is the calculation by O'Brien [31].

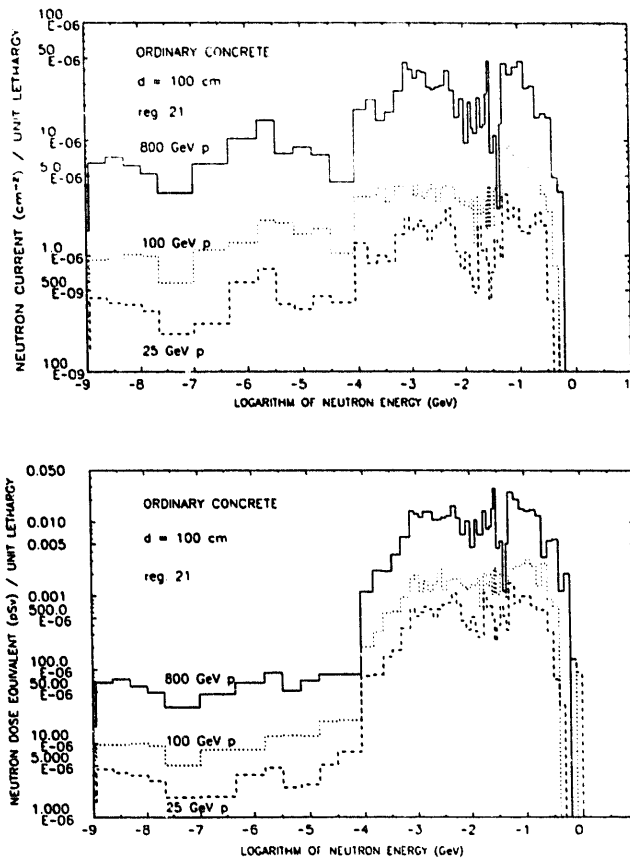


Fig. 6. Comparison of neutron current spectra and neutron dose spectra, normalized per primary proton, for 3 different beam energies.

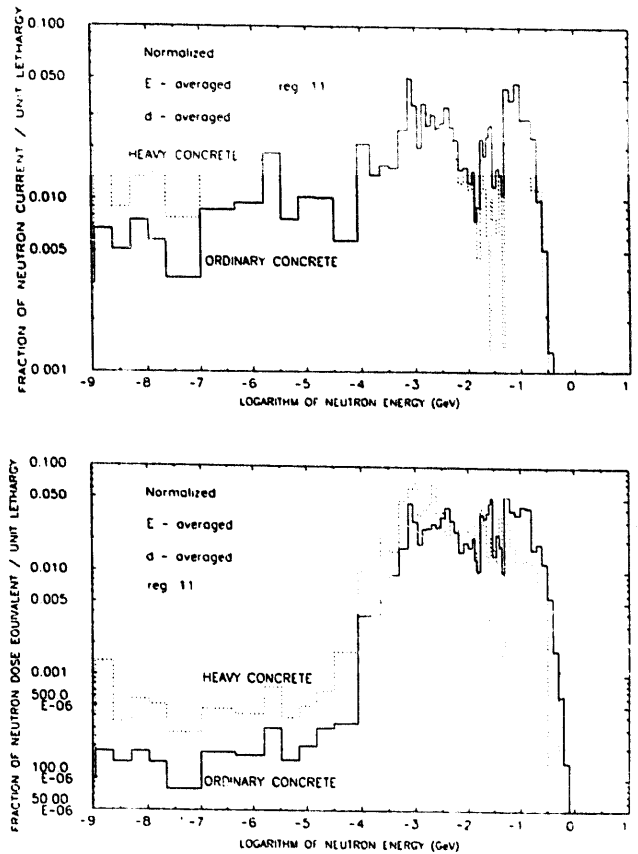


Fig. 7. Comparison of averaged neutron current spectra and neutron dose spectra, normalized to unity, for 2 different types of concrete.

and then averaged over d and E values. The high contribution from neutrons between 0.5 and 10 MeV is apparent. This is due to the evaporated neutrons, and, for the dose equivalent, to the additional increase of the conversion factors in that energy range. Another im-

portant contribution due to neutrons between 50 and 200 MeV is remarkable, more pronounced in the case of ordinary concrete and for the forward directions; and it should be accounted for when selecting methods of neutron dosimetry. Behind the heavy concrete shields,

Table 10

Averaged fractions of dose equivalent estimated from emerging currents (H_J) and from dose absorbed (H_D), as contributed by different secondary radiation components

Particles	Fraction of H_J		Fraction of H_D	
	Ordinary concrete	Heavy concrete	Ordinary concrete	Heavy concrete
e.-m. cascade	a) -	-	0.008	0.008
High en. + evap. p	0.010	0.007	0.031	0.031
Charged π	0.012	0.011	0.018	0.014
Evap. $\alpha, d, t, {}^3\text{H}$ + rec.	b) -	-	0.116	0.100
High en. n ($E > 50$ MeV)	0.278	0.161	c) -	-
n (50 MeV $> E > 20$ MeV)	0.101	0.095	0.105	0.105
n (20 MeV $> E > 500$ keV)	0.510	0.553	0.468	0.439
Slow + th. n ($E < 500$ keV)	0.102	0.185	0.277	0.334

a) Not calculated here.

b) Not occurring here.

c) Included in absorbed dose of charged secondaries.

Table 11
Total dose equivalent (Sv) per primary proton behind ordinary concrete shields

$d(\text{cm})$	^{a)} Reg. 6	Reg. 11	Reg. 16	Reg. 21
$E_p = 25 \text{ GeV}$				
100	9.8-16(0.10) ^{b)}	2.1-15(0.06)	2.8-15(0.05)	2.3-15(0.06)
150	1.2-16(0.11)	3.6-16(0.08)	5.4-16(0.06)	4.6-16(0.07)
200	2.5-17(0.17)	1.0-16(0.11)	1.1-16(0.09)	1.5-16(0.09)
250	1.6-18(0.28)	2.7-17(0.19)	2.2-17(0.16)	3.1-17(0.15)
$E_p = 100 \text{ GeV}$				
100	1.8-15(0.13)	6.0-15(0.06)	6.4-15(0.05)	5.5-15(0.06)
150	5.2-16(0.15)	9.5-16(0.08)	1.5-15(0.06)	1.4-15(0.07)
200	8.2-17(0.25)	1.9-16(0.13)	3.8-16(0.09)	2.8-16(0.10)
250	2.7-17(0.33)	5.2-17(0.21)	6.9-17(0.17)	1.2-16(0.15)
$E_p = 800 \text{ GeV}$				
100	1.2-14(0.11)	2.4-14(0.06)	4.0-14(0.07)	3.7-14(0.07)
150	2.2-15(0.15)	4.8-15(0.07)	8.7-15(0.08)	7.4-15(0.07)
200	3.8-16(0.21)	8.8-16(0.13)	2.1-15(0.11)	1.9-15(0.13)
250	1.1-16(0.39)	1.9-16(0.22)	5.0-16(0.17)	4.0-16(0.14)

^{a)} See fig. 4 for geometry region layout.

^{b)} Read as $9.8 \times 10^{-6} \pm 10\%$ fractional standard deviation.

the portion of neutrons above 50 MeV is reduced and the contribution of neutrons below 0.5 MeV is increased by a factor of two compared to ordinary concrete. This is due to the iron content which removes high energy neutrons more efficiently than light elements, but is more transparent to neutrons in the keV energy range. Below 100 keV, the spectra have a more or less flat character (note the normalization to unit lethargy), which is the typical $1/E$ slowing down behavior.

5.4. Dose equivalents

The relative fractions of the total dose equivalents, contributed from different neutron energy ranges, averaged over shield thicknesses and beam energies (for the tissue region 16), are given in table 10, together with approximate fractional dose equivalents of the electromagnetic cascade and charged particles. The main contribution is due to neutrons, as expected. The absorbed dose is also dominated by products of the intermediate neutron reactions; the contribution from cascade protons and pions and from evaporated charged particles are one order of magnitude lower.

When estimating the dose equivalent by using particle currents entering the tissue (H_J), only long-range particles emerging from a shield are important, and contributions to the total dose from other than the neutron components clearly do not exceed a few percent. Note that the secondary charged particles from a hadronic cascade or from evaporation within the tissue should not be considered when using this method, since they have already been included in the fluence-to-dose conversion factors. When estimating the dose equivalent by deposited energy and the quality factors (H_D), the

charged products of evaporation contribute about 10% of the total dose equivalent (note the high quality factor of 20 for evaporated heavy fragments and recoiling residuals). The significant differences between the dose components for ordinary and heavy concrete shields are visible only when considering the doses due to particles entering tissue from outside.

For completeness, the absorbed dose of the electromagnetic cascade was added to the total dose equivalents presented in tables 7-12, with quality factor equal to 1. We have already mentioned that doses due to photons from inelastic scattering and radiative capture of neutrons and from deexcitation of nuclei after evaporation are not calculated. From the previous calculations [10] we can estimate the γ dose from neutron scattering and capture to be roughly 10% of the neutron dose equivalent behind ordinary concrete and much less behind heavy concrete. The dose due to photons from evaporation and spallation is unknown at present.

The total dose equivalents (mean values obtained from the two methods), versus region, shield thickness and beam energy, are listed in table 11 for ordinary concrete and in table 12 for heavy concrete. The statistical errors (standard deviations of the results from several batches) included in parenthesis are those obtained for the currents; it can be argued that the relative statistical errors of the dose equivalents are nearly the same.

The maximum of dose equivalent along the shielding wall can be compared with earlier results [1] by using eq. (1). We used the total dose equivalent calculated in region 16 as the maximum value. The position and magnitude of the maximum could be determined more accurately (e.g., a factor of 0.58 was found between the

Table 12
Total dose equivalent (Sv) per primary proton behind heavy concrete shields

d(cm)	a) Reg. 6	Reg. 11	Reg. 16	Reg. 21
$E_p = 25 \text{ GeV}$				
50	7.9-15(0.05) ^{b)}	1.9-14(0.02)	1.7-14(0.04)	1.1-14(0.06)
100	5.7-16(0.12)	1.4-15(0.07)	1.9-15(0.07)	1.4-15(0.09)
150	6.5-17(0.24)	1.8-16(0.14)	2.4-16(0.12)	2.1-16(0.15)
200	3.5-18(0.40)	2.0-17(0.30)	5.1-17(0.22)	3.1-17(0.25)
$E_p = 100 \text{ GeV}$				
50	2.4-14(0.04)	4.8-14(0.03)	4.6-14(0.03)	3.5-14(0.08)
100	1.1-15(0.12)	2.8-15(0.08)	5.4-15(0.09)	4.1-15(0.04)
150	7.4-17(0.28)	5.4-16(0.14)	6.3-16(0.09)	6.1-16(0.15)
200	9.5-18(0.29)	1.1-16(0.26)	1.4-16(0.24)	1.2-16(0.23)
$E_p = 800 \text{ GeV}$				
50	1.1-13(0.04)	2.8-13(0.03)	3.1-13(0.01)	1.9-13(0.01)
100	5.3-15(0.14)	1.7-14(0.12)	3.6-14(0.10)	2.6-14(0.10)
150	6.5-16(0.30)	2.3-15(0.16)	3.0-15(0.16)	3.3-15(0.20)
200	5.7-17(0.31)	1.7-16(0.23)	4.6-16(0.21)	4.6-16(0.11)

a) See fig. 4 for geometry region layout.

b) Read as $7.9 \times 10^{-15} \pm 15\%$ fractional standard deviation.

longitudinally averaged and the maximum energy density in region 16, for 25 GeV protons and 50 cm heavy concrete shield), but since it is only weakly pronounced we decided not to spend the additional computing time.

After eliminating the $E_p^{0.8}$ power law and the r^{-2} dependence, the dose equivalents show the expected exponential decrease with thickness d (see fig. 8). For ordinary concrete the two parameters resulting from the regression fit are $H_0 = 0.87 \times 10^{-14} \text{ Sv m}^2$ and $\lambda = 107 \text{ g cm}^{-2}$. They agree well with the values given previously. For the maximum dose equivalent behind heavy concrete we received $H_0 = 1.6 \times 10^{-14} \text{ Sv m}^2$ in agreement with the previous approximation, but the resulting attenuation length $\lambda = 116 \text{ g cm}^{-2}$ is considerably lower than given before. In our earlier calculations [1] using the FLUKA82 code (with 50 MeV energy cutoff) we had got $\lambda = 134 \text{ g cm}^{-2}$, this value is close to $\lambda_S = 127$

g cm^{-2} obtained now for the star density attenuation length in heavy concrete (50 MeV is the threshold for scoring star density also in FLUNEV). We should also emphasize that an essential λ dependence on the angle relative to the beam axis has been reported from the previous MC calculations [3]; for our geometry, a similar fit for the dose attenuation in the more forward region 21 gave $\lambda = 125 \text{ g cm}^{-2}$ for heavy concrete. In contrast to these values, the only measurements performed with heavy concrete and a 12 GeV beam gave the much higher value of $\lambda = (163 \pm 7) \text{ g cm}^{-2}$ [2,27].

The FLUNEV results of the present work should be more reliable than the results of the original FLUKA since the production and transport of low energy neutrons are taken into account and more recent conversion factors and kerma factors are used. We see no reasons why results obtained for heavy concrete should be less reliable than for ordinary concrete. Therefore we believe that eq. (1) with our parameters given above can be used for calculating doses behind ordinary or heavy concrete shielding.

Acknowledgement

We wish to express our gratitude to our colleague Dr. H. Dinter for his interest and for fruitful discussions.

References

[1] K. Tesch and H. Dinter, Radiat. Protect. Dos. 15 (1986) 89.

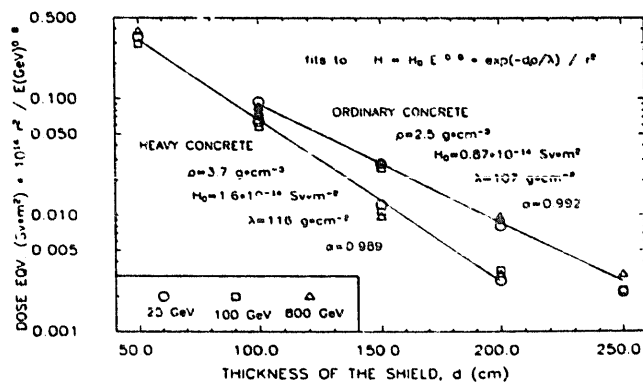


Fig. 8. Fits of total dose equivalents in tissue region 16 to the attenuation formula, eq. (1), for ordinary concrete and heavy concrete (the obtained regression coefficients are indicated as α values).

- [2] R.H. Thomas and G.R. Stevenson, IAEA Technical Report Series, No. 283, Vienna (1988).
- [3] H. Dinter, K. Tesch and C. Yamaguchi, Nucl. Instr. and Meth. A276 (1989) 1.
- [4] G.R. Stevenson, K.L. Liu and R.H. Thomas, Health Phys. 43 (1982) 13.
- [5] G.R. Stevenson, CERN Report TIS-RP/173 (1986).
- [6] F.S. Alsmiller and R.G. Alsmiller, Jr, Oak Ridge National Laboratory Report ORNL/TM-11032 (1985).
- [7] R.G. Alsmiller, Jr, T.A. Gabriel and J. Barish, Nucl. Instr. and Meth. 155 (1978) 399.
- [8] T.A. Gabriel and R.S. Santoro, Nucl. Instr. and Meth. 95 (1971) 275.
- [9] A. Ferrari, A. Fasso and C. Sirttari, CERN Report TIS-RP/211/CF (1988).
- [10] J.M. Zazula, D. Filges and P. Cloth, Part. Accel. 21 (1987) 29.
- [11] J.M. Zazula, P. Cloth, D. Filges and G. Sterzenbach, Nucl. Instr. and Meth. B16 (1986) 506.
- [12] R.S. Caswell and J.J. Coyne, Radiat. Res. 83 (1980) 217.
- [13] P. Cloth, D. Filges, G. Sterzenbach, T.W. Armstrong and B.L. Colborn, KFA Jülich Report Jül-Spez-196 (1983).
- [14] T.A. Gabriel, Oak Ridge National Laboratory Report ORNL/TM-9727 (1985).
- [15] P.A. Arnio, J. Lindgren, J. Ranft, A. Fasso and G.R. Stevenson, CERN Report TIS-RP/190 (1987).
- [16] M.B. Emmet, Oak Ridge National Laboratory Report ORNL-4972 (1975).
- [17] M.A. Abdou, C.W. Maynard and R.Q. Wright, Oak Ridge National Laboratory Report, ORNL/TM-3994 (1973).
- [18] W.R. Nelson, H. Hirayama and D.W. Rogers, Stanford Linear Accelerator Center Report, SLAC-265 (1985).
- [19] T.A. Gabriel, J.E. Brau and B.L. Bishop, Oak Ridge National Laboratory Report ORNL/TM-11060 (1989).
- [20] P. Cloth, D. Filges, R.D. Neef, G. Sterzenbach, Ch. Reul, T.W. Armstrong, B.L. Colborn, B. Anders and H. Brückmann, KFA Jülich Report Jül-2203 (1988).
- [21] H. Kowalski, H.-J. Moehring and T. Tymieniecka, Deutsches Elektronen-Synchrotron Report DESY 87-170 (1987).
- [22] W.W. Engle, Jr, USA Atomic Energy Commission Report, USAEC/K-1693 (1969).
- [23] W.A. Rhoades, Oak Ridge National Laboratory Report ORNL-6529 (1978).
- [24] D. Garber, Brookhaven National Laboratory Report, BNL/NCS-17541 (1975).
- [25] R.G. Alsmiller, Jr and J. Barish, Nucl. Sci. Eng. 80 (1982) 448.
- [26] R.G. Alsmiller, Jr, J.M. Barnes and J.D. Drischler, Nucl. Instr. and Meth. A249 (1986) 445.
- [27] S. Ban, H. Hirayama, K. Kondo, S. Miura, K. Hozumi, M. Taino, A. Yamamoto, H. Hirabayashi and K. Katoh, Nucl. Instr. and Meth. 174 (1980) 271.
- [28] International Commission on Radiological Protection, ICRP Publication No. 21 (Pergamon Press, Oxford, 1971).
- [29] International Commission on Radiological Protection, ICRP Publication No. 51 (Pergamon Press, Oxford, 1987).
- [30] International Commission on Radiological Units, ICRU Publication No. 39 (Pergamon Press, Oxford, 1935).
- [31] K. O'Brien, Health and Safety Laboratory Report, HASL-240, New York (1971).